



Transition zone parameter development in multi-material powder bed fusion: a general approach

Timo Schroeder¹ · Maja Lehmann^{1,2} · Max Horn^{1,2} · Philipp Kindermann¹ · Ismail Uensal¹ · Florian Michal¹ · Anja Lippus¹ · Georg Schlick¹ · Christian Seidel^{1,3}

Received: 2 May 2024 / Accepted: 7 May 2024 / Published online: 28 May 2024
© The Author(s) 2024

Abstract

Power bed fusion of metals using a laser beam (PBF-LB/M) offers unique possibilities to manufacture functionally graded materials (FGM) consisting of different alloys. These so-called multi-material parts enable their material properties to be tailored to local material requirements. In this paper, a new methodical approach for the production of metal FGM with transition zones oriented in different directions and manufacturing sequences of the different materials is investigated. Existing approaches for the manufacturing of these transition zones were enhanced with graded parameter variations, spatial laser movement modulation techniques (wobbling), and geometric approximations using a step structure. For the validation of the approach and the characterization of the transition zones, the manufactured samples were investigated and characterized using optical microscopy and hardness profile measurements. Furthermore, the density of the transition zones was analyzed by image data processing. The feasibility of the presented methods is shown and the production of defect-free transition zones with controlled expansions for functionally graded materials via PBF-LB/M achieved

Keywords Multi-material · Additive manufacturing · Interface · PBF-LB/M · Functionally graded materials

1 Introduction

1.1 Multi-material manufacturing

Functionally graded materials (FGM) are the key for mastering the challenging requirements of today's high-tech applications. By varying the material composition throughout a component, the FGM-subgroup of compositionally graded materials (CGM), also referred to as multi-material components, enables a deliberate and purposeful allocation of the

material properties [1, 2]. Examples include the combination of optimal strength or high temperature resistance and thermal conductivity [3–5], hardness and toughness [6, 7], sensor integration [8] as well as mechanical properties and high biocompatibility [9]. This contributes to the development of more adaptable products with a higher performance density and allows a more efficient and sustainable use of critical materials.

Due to its degrees of freedom during the manufacturing process, the achievable part resolution, and its widespread use, the additive manufacturing (AM) process of laser powder bed fusion (PBF-LB/M) is especially relevant for the creation of metal-based CGMs [1, 2, 8, 10]. PBF-LB/M builds components by solidifying a powder feedstock in its cross section layer by layer. A single layer of powder is spread onto a build platform and the laser beam melts the powder particles in each layer [11]. Schneck et al. [1] reviewed recent advancements in PBF-LB/M for manufacturing CGMs. According to the researchers, the geometrical representation of the material transition zone as well as the development of the transition zone process parameters and their allocation in the digital model remain key challenges for the multi-material PBF-LB/M process.

✉ Timo Schroeder
Timo.schroeder@igcv.fraunhofer.de

¹ Fraunhofer Institute for Casting, Composite and Processing Technology IGCV, Am Technologiezentrum 10, Augsburg 86159, Germany

² Department of Mechanical Engineering, TUM School of Engineering and Design, Institute for Machine Tools and Industrial Management, Technical University of Munich, Boltzmannstrasse 15, Garching 85748, Germany

³ Department of Applied Sciences and Mechatronics, Munich University of Applied Sciences, Lothstr. 34, Munich 80335, Germany

1.2 Transition zone

The majority of existing studies either investigated the manufacturing process itself or the general process behavior and occurring defects for certain material combinations [1]. Approaches included, e.g., the explanation of general process implications [12], melt pool simulations of powder mixtures [13], or collections of predominant defects [14]. As different materials demand different energy inputs, the mono-material regions of CGMs are scanned with different process parameters [1]. If the energy input differs significantly, either too much or not enough energy is applied in the transition zone, which may cause keyhole porosity or lack of fusion defects [15]. This is especially relevant for the material transition in the vertical direction (z-direction) [16]. Furthermore, unfavorable material compositions or melt pool shapes and sizes in the transition zone might support further defects, such as hot cracking [4, 17]. For material transitions in the horizontal direction (in the x–y plane), previous research [16, 18, 19] suggested the scan vectors of the different materials should overlap to secure a proper material bond. If the overlap is too wide, however, the excessive heat input during the double exposure may cause defects and undesired material inclusions.

However, hardly any studies exist on how to minimize or fully mitigate occurring transition zone defects. Anstaett [16] derived transition zone scanning parameters from processing of powder mixtures composed of equal parts of the desired materials. Her method gives an indication for the general process window, but does not account for the necessity of angle-dependent processing strategies and parameters. It was found that if a universal scan strategy and process parameter are applied to the transition zones of all angles, for many material combinations, the type of observable defects may vary significantly [3, 4].

Rankouhi et al. [20] suggested using machine learning algorithms to predict suitable multi-material process parameters, also for transition zones in different build angles. Even though the approach appears promising, it was not pursued into a product or method and is therefore not generally applicable by academia or industry. Thus, both existing approaches do not yet fully meet the demands for multi-material PBF-LB/M.

1.3 The combination of steel and copper

The material combination of tool steel and copper alloys is the most investigated one in the literature [1]. To provide an overview of the challenges of this material combination employed in PBF-LB/M, the characteristics inherent to the

combination of the tool steel 1.2709 (X3NiCoMoTi18-9-5) and the copper alloy CW106C (CuCr1Zr) are briefly summarized based on Horn et al. [17]. The Fe–Cu binary system exhibits a peritectic reaction for the Fe-rich side, a flat liquidus line, and a complete solid state immiscibility. At approximately 1450 °C, γ -Fe has the highest solubility of Cu, exceeding 11% [21]. Due to the low absorptivity of Cu alloys in the infrared wavelength, much higher-energy inputs are necessary than that commonly used for steels [20, 22], which may cause keyhole porosity or lack of fusion defects [15]. The combination of these materials shows a liquid-phase separation during the rapid solidification, resulting in dispersed droplets of both components. Depending on the concentration of the elements and the cooling rates, secondary and tertiary phase separations may occur, leading to the presence of distinct Fe-rich and Cu-rich zones [23–27]. Thus, in laser-welded dissimilar metal joints, such as low-alloy, stainless, and tool steels with Cu alloys, the fusion zones are characterized by discrete ϵ -Cu and γ -Fe or α -Fe zones. The discrete accumulation of the liquefied Cu along already solidified grain boundaries in steel materials can result in hot cracking [24, 27–29]. These effects were also observed when the material combination was processed via PBF-LB/M in previous investigations [4, 16, 19].

1.4 Interim conclusion and approach

Currently, no method exists to address the challenges of the PBF-LB/M process parametrization with regard to the transition zones with varying orientations for a material combination with a strong variation of the energy input. In PBF-LB/M, the laser power is always applied vertically to each layer of the powder bed at an angle close to 90°. The resulting staircase effect is especially relevant for the inclined material transition zones, as different energy inputs and scan vector overlaps might be required for different angles.

This study introduces a methodical approach for manufacturing defect-free transition zones in multi-material PBF-LB/M using the example of a tool steel and a copper alloy. The layerwise fabrication of a component is exploited to enable the generation of the desired material interfaces with almost identical dimensions and mechanical properties, regardless of their orientation and geometry. The application is particularly useful if the standard parameters differ greatly in regard to the energy input.

2 Methodical approach

The optimization of the transition zone is associated with a high experimental effort. The aim of this approach is to reduce the number of transition zones in conjunction with

different process parameters and limit them to only two orientations. The underlying mechanism is the layerwise manufacturing of a component during PBF-LB/M and the resulting stair step effect. The geometry of a component is sliced into individual layers, which are stacked to build the 3D part. When a geometry contour changes its angle to the build direction (z -direction), a step is created. The smallest possible step is the chosen layer height of the manufacturing process.

A transition zone between two different materials (material A and material B) in multi-material PBF-LB/M can also be interpreted as a geometry contour. Representing the transition zone by a stair results in two different material transition orientations: a horizontal (x - y plane) and a vertical interface (z -direction) (see Fig. 1).

The step height corresponds to the layer thickness or its integer multiple. The width depends on the angle to the build direction. The flatter the angle, the wider do the steps have to be (angle measured counterclockwise starting from the x -axis). Thus, for the production of a multi-material component, three transition zones have to be optimized to create defect-free intersections. The build strategies and the associated process parameters for the following build sequences have to be investigated: material A on material B, material B on material A, and material A and B next to each other. Additionally, the combination of the vertical and horizontal transition zones and the size of the stairs have to be evaluated. The approach is valid for two materials: when the main alloying elements are weldable together and the liquidus temperature of one material does not lie above the evaporation temperature of the other material. For filigree structures and thin walls, adaptations have to be made. In the following, the concept for the manufacturing of each direction of the transition zones and their combination is outlined.

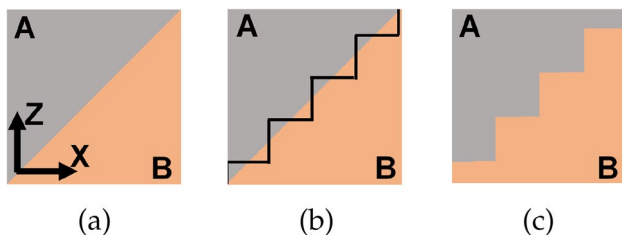


Fig. 1 Theoretical approach for manufacturing the transition zones between two different materials (material A and material B) with steps by the discretization into vertical and horizontal transition zones, **a** reference transition zone, **b** theoretical steps, **c** discretized transition zone

2.1 Transition zones in the z -direction

In the horizontal direction, a defect-free transition zone independent of the build sequence of the two materials has to be generated. A direct buildup of the two materials with the standard parameters induces either too little or too much energy into the material in the layers directly after the material transition, which leads to defects and unevenly shaped melt pools. Thus, an adaptation of the standard process parameter is required within the layers in the transition zone. For this approach, a graded transition between the energy densities of the two materials was chosen and the energy input was adjusted linearly. The standard parameters are used to calculate the volumetric energy density E [30], which can be expressed as

$$E = \frac{P}{dhv}, \quad (1)$$

with the laser power P , the layer thickness d , the hatch spacing h , and the scan speed v , and indicates the energy input into a material. The layer thickness has to be equal for the standard parameters of both materials. The difference between the volumetric energy density of the two materials is interpolated by a linear function (see Fig. 2).

This function defines the energy input for each layer in the transition zone. The laser power and the hatch distance are linearly interpolated, and the scan speed is calculated to achieve the linear variation of the volumetric energy density from material A to material B. The number of layers is determined by the energy difference. Depending on the build sequence of the materials, the number of layers varies due to the varying depths of the melt pools. The aim is to achieve a trade-off between minimized defects and a transition zone with low vertical expansion. The more the layers are selected, the wider does the transition zone become. The properties of these are difficult to define. Too few layers lead to defects. The exact number of layers is identified experimentally; however, it can vary depending on the build strategy. When the material with the higher-energy input is built on the material with the lower-energy input, comparatively more layers are required to obtain the same expansion with no defects of the transition zone than vice versa. Therefore, to obtain a suitable number of layers for the transition zone, the material with the higher-energy input is built sequentially with increasing number of layers on the other material following the linear interpolation. The smallest number of layers and, thus, the minimal expansion, in which no defects occurred, was selected. The number of layers for the other build sequence is chosen to ensure that the transition zones achieve the same expansion. With this method, a graded energy input is introduced into the transition zone from the bulk

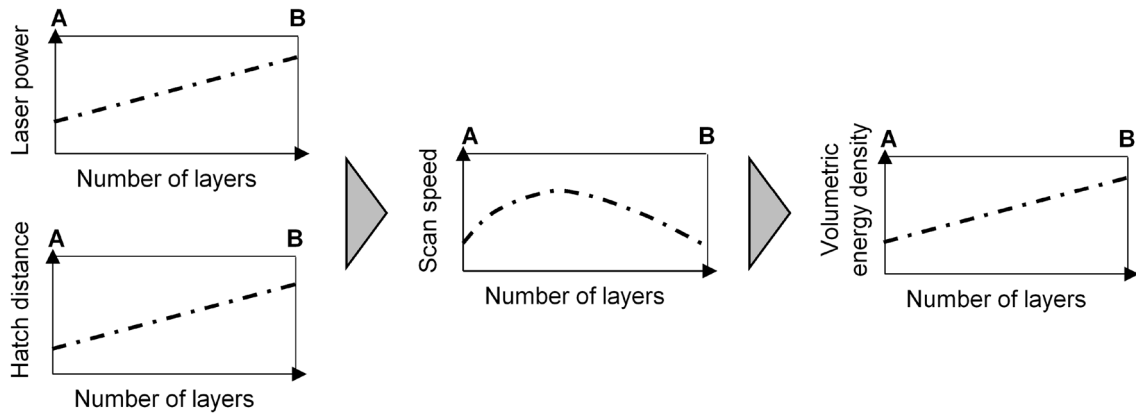


Fig. 2 Linear interpolation of the volumetric energy density between the materials A and B; the laser power and the hatch distance are linearly interpolated, the scan speed is calculated accordingly to obtain a

linear course of the volumetric energy density, and the layer thickness remains constant

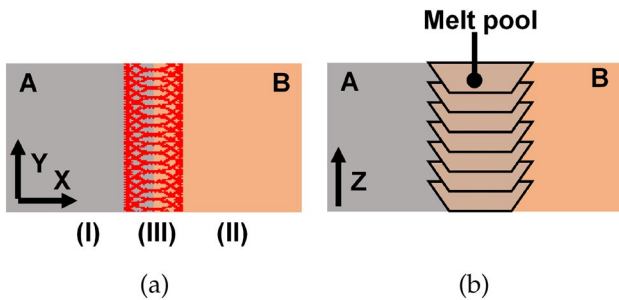


Fig. 3 **a** Wobble geometry for the transition zone in the x–y plane, I–III: sequence of the exposure (I) material A with the lower-energy input, (II) material B with the higher-energy input, (III) material transition zone scanned with the wobbling strategy, **b** desired melt pool in the transition zone as a result of the wobbling scan strategy

material fabricated with standard parameters at the bottom to the other bulk material manufactured with its standard parameters at the top.

2.2 Transition zones in the x–y plane

Materials A and B are built adjacent to each other without any overlapping scanning vectors. The bonding between the two materials is ensured by a third scan with a different set of parameters. A beam trajectory with a circular beam oscillation, also known as *wobbling*, is applied [31, 32] (see Fig. 3a).

The width of the wobbling movement can be varied, which allows to control the expansion of the transition zone. The wobbling path creates a wide and homogeneous melting front (see Fig. 3b) in which the two materials intermix in a liquid state. Thus, the solidification occurs slower, which serves to reduce the hot cracks.

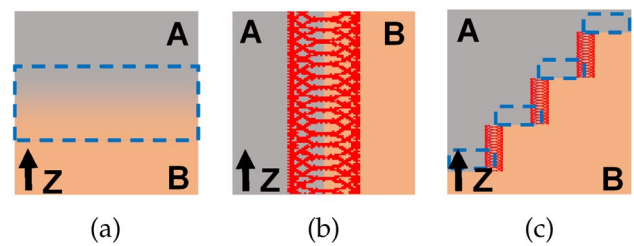


Fig. 4 Scanning strategy for the three-dimensional (3D) transition zone, **a** transition zones in the z-direction with graded energy input, **b** transition zones in the x–y plane with the wobbling strategy, **c** discretized transition zone using steps for the combination of the transition zones in the z-direction and in the x–y plane

2.3 Combined strategies for three-dimensional transition zones

The aforementioned strategies are combined to obtain transition zones with nearly identical dimensions and properties regardless of the build direction and the angle of the transition zone. For the overarching build strategy, the original geometry is divided into height-defined steps. In theory, the maximum possible accuracy would be the minimum step height resulting from the required additional parameter layers of the build strategy in the z-direction (cf. Sect. 2.1). The step height considered is the layer thickness or its integer multiple. The greater the step height, the higher is the deviation from the original transition contour and the poorer is the accuracy of the strategy. However, using too small steps can lead to an interference of the two different build strategies and might result in unpredictable process interactions.

In Fig. 4, the build strategies for the two directions and their combination for any angle are depicted.

Table 1 Particle size distributions

Material	$x_{10,3}$ in μm	$x_{50,3}$ in μm	$x_{90,3}$ in μm
1.2709	21	32	49
CW106C	19	30	44

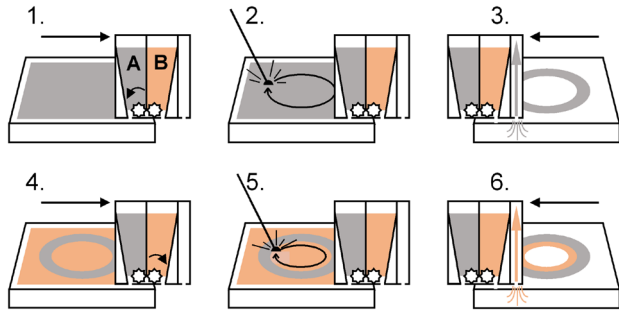


Fig. 5 Schematic representation of the multi-material PBF-LB/M process based on Anstaett [16] and Schneck et al. [3]

The blue dashed line marks the area, which was manufactured with the parameter set for the linear interpolation from Sect. 2.1. The red trajectory is the path, the wobbling strategy takes in the transition zone for the x–y plane. In Fig. 4c, both strategies are allocated to their areas. The wobbling trajectory starts several layers after the beginning of the build strategy in the z-direction to avoid an overlapping of the two different strategies.

3 Experimental procedure

The listing of the materials and methods used in this study is based on VDI guideline 3405 Part 2.6 [33]. Two powder blends were employed—the copper alloy CW106C and the tool steel 1.2709. In accordance with VDI guideline 3405 Part 2.6 [33], their status can be defined as 2B (used powder blend). The particle size distribution (PSD) values for the diameters x at goods receipt were measured by laser diffraction using a Mastersizer3000 (Malvern Panalytical, UK) and are listed in Table 1.

All samples were manufactured on a customized SLM 280^{HL} PBF-LB/M machine (Nikon SLM Solutions AG, Germany). The system has a divided recoating system and a suction unit to apply and remove different powder materials as described by Anstaett [16].

After applying (1.) and solidifying the first material (2.), it is removed by the suction unit (3.) and the second material can be deposited (4.) and solidified (5.) without moving the z-axis. Only after the second material is removed by the suction unit (6.), the build platform is lowered and the process is repeated for the next layer (see Fig. 5).

Table 2 Standard process parameters

Parameter	1.2079	CW106C
Laserpower	200 W	450 W
Scan speed	800 mm/s	800 mm/s
Hatch distance	120 μm	130 μm
Layer thickness	30 μm	30 μm
Vol. energy density	69.44 J/mm ³	144.23 J/mm ³

Table 3 Wobbling parameters used for the transition zone in the x–y plane

No. #	Laser power in W	Scan speed in mm/s	Scan path radius in mm
1	100	800	0.250
2	100	800	0.125
3	100	1600	0.250
4	100	1600	0.125
5	100	2400	0.250
6	100	2400	0.125
7	75	2400	0.250
8	75	2400	0.125

According to the comparison conducted by Schneck et al. [1], this multi-material system is the only solution in which the achievable powder deposition resolution and accuracy does not depend on limitations from the multi-material powder deposition system itself and was, therefore, selected for this study. Argon was used as inert gas and a silicone rubber lip as a recoating device.

The standard process parameters used for the two materials are summarized in Table 2.

For the validation, various cuboid samples were prepared with two different build sequences (CW106C build on 1.2079 and vice versa) with transition zones in the z-direction. Also samples with their transition zones in the x–y plane were fabricated using the approach from Sect. 2.1 with the graded energy input in the transition zone.

For the wobbling strategy in the x–y plane, two approaches were applied. A wider and a narrower scan path radii were chosen for the circular trajectory. Different parameter sets with decreasing energy input were studied starting with parameters with the laser power slightly reduced compared to the tool steel parameter set, while the scan speed remained the same. The parameters are shown in Table 3.

Additionally, reference samples were manufactured with two different reference strategies, which are commonly employed for the manufacturing of multi-material components:

- **Strategy *No overlap***: the transition zones in the z-direction were built with no overlapping regions of the materials and with the use of the standard parameters.
- **Strategy according to Anstaett [16]**: the transition zone was manufactured with an overlap of the scan vectors of the two materials of 0.2 mm in the x–y plane without any adaption of the process parameters.

Beyond the horizontal (z-direction) and the vertical (x–y plane) material transition zone, three additional transition zone angles were fabricated for the validation of the 3D transition zones: 22.5°, 45°, and 67.5°. For each angle, three different step heights of 0.3 mm, 0.6 mm, and 0.9 mm were applied. To compare the presented approach with the approach from Anstaett [16], reference samples for each transition zone were manufactured accordingly. Furthermore, a sample at the angle of 45° was fabricated with the no overlap strategy. After the manufacturing, the samples were cut from the build plate using wire electrical discharge machining without a heat treatment to limit the influences in the metallurgical structure in the transition zone. Some of the prepared cross sections were etched using V2A etchant for 45 s.

A BX53M (Olympus, Japan) upright visual light microscope (VLM) was used for qualitative and quantitative analysis of the transition zones, including optical density measurements based in VDI 3405 Part 2 [34]. The investigated area was defined as 500 μm perpendicular to the transition zone and the density was analyzed using the software ImageJ [35].

The width of the transition zone was determined based on the hardness profile measurements, which were carried out perpendicular to the material transition zone with a ZHUZ2.5 (Zwick Roell, Germany) machine according to DIN EN ISO 6507-1 [36]. The Vickers hardness (VHN) HV1 was selected to secure a comparability of the two materials, which have significant differences in hardness. The distances between the test indents were chosen to avoid any interference between the individual indents, as recommended by the standard. To ensure that the hardness progression perpendicular to the transition zone was mapped in as much detail as possible, the indents were placed in several rows and at shifted distances from the transition zone. The beginning and the end of the transition zone were defined along the hardness profile at a deviation of 10% from the hardness of the respective monolithic material region (90% VHN of 1.2709 and 110% VHN of CW106C).

4 Validation and discussion

4.1 Transition zones in the z-direction

The expansion of the transition zones was set by the definition of the minimum number of layers with graded energy

Table 4 Graded energy input for four layers (1.2709 on CW106C)

Layer	Laser power in W	Scan speed in s	Hatch distance in μm	Vol. energy density n J/ mm^3
0	450	800	130	144.2
1	388	807	128	125.2
2	325	811	125	106.9
3	263	811	123	87.9
4	200	800	120	69.4

Table 5 Graded energy input for ten layers (CW106C on 1.2709)

Layer	Laser power in W	Scan speed in mm/s	Hatch distance in μm	Vol. energy density n J/ mm^3
0	200	800	120	69.4
1	225	806	121	76.9
2	250	809	122	84.4
3	275	811	123	91.9
4	300	812	124	99.4
5	325	811	125	106.8
6	350	810	126	114.3
7	375	808	127	121.8
8	400	806	128	129.3
9	425	803	129	136.8
10	450	800	130	144.2

input for the fabrication of CW106C on 1.2709. No defects were detected in the transition zone after ten layers with graded energy input. For the manufacturing of 1.2709 on CW106C, a defect-free transition zone was obtained after four layers with a graded energy input. The successive layers were built with their respective energy inputs. For four and ten layers, the employed parameters and the calculated volumetric energy densities are listed in Tables 4 and 5.

In Fig. 6, the micrographs of the transition zones for the manufacturing of CW106C on 1.2709 and vice versa are depicted.

The images show the reference samples (see Fig. 6a and c) and the samples manufactured with the optimized strategy (see Fig. 6b and d).

The transition zone in Fig. 6a exhibits that the gas porosity and the intermixing area of the two materials is wider than for the transition zone manufactured with the optimized strategy (see Fig. 6b). In contrast, the transition zone in Fig. 6c is nearly discrete. The exemplary close-up of the reference transition zone in Fig. 7 reveals the formation of hot cracks in the material region of 1.2709 next to the interface.

With the optimized strategy, the transition zones for both build strategies show similar expansions and material

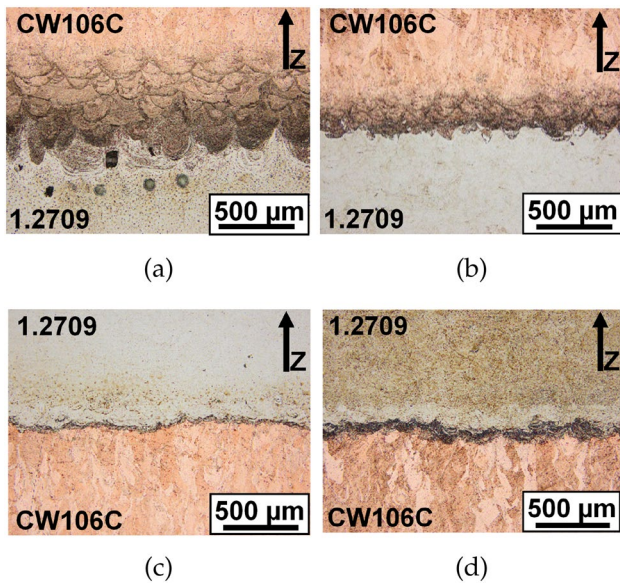


Fig. 6 Micrographs of the material transition zone in the z-direction, **a** reference strategy *No overlap* for CW106C on 1.2709, **b** optimized strategy for CW106C on 1.2709, **c** reference strategy *No overlap* for 1.2709 on CW106C, **d** optimized strategy for 1.2709 on CW106C

intermixing (see Fig. 6b and d) and are nearly defect free. No cracks were observed.

The width of the transition zones was determined using the Vickers hardness as described in Sect. 3. In Fig. 8, the hardness values for CW106C build on 1.2709 are plotted over the position perpendicular to the transition zone. Two curves are shown in the plot. A reference for the standard strategy according to Anstaett [16] and the values obtained with the optimized strategy.

Both curves show similar values in the monolithic material regions of CW106C and 1.2709. The hardness

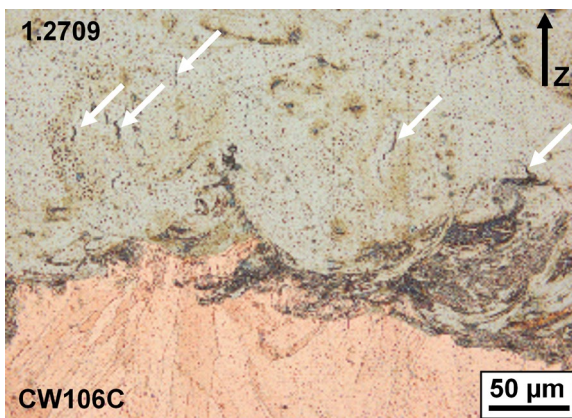


Fig. 7 Exemplary micrograph of the material transition zone in the z-direction (1.2709 on CW106C) manufactured with the reference strategy; the hot cracks are marked by the white arrows

in the 1.2709 monolithic material region exhibits slight deviations, while for CW106C constant values could be measured. The grains in the 1.2709 regions differ in size and due to the small load of HV1, these deviations occurred.

A difference of the course is apparent in the width of the transition zone. For the reference it starts at a position of -0.283 mm and intersects the threshold (dotted-dashed line) at 0.612 mm. This results in a width of 0.895 mm. The transition zone fabricated with the optimized strategy is 0.315 mm wide. It starts at -0.096 mm and ends at 0.219 mm.

Building 1.2709 on CW106C shows only slight differences in the width of the transition zones between the reference sample and the optimized strategy (see Fig. 9).

The values in the monolithic regions of 1.2709 and CW106C exhibit the same behavior as for the other build sequence. The transition zone of the reference sample starts at -0.091 mm and crosses the 10% threshold of the hardness at 0.270 mm. This results in a width of 0.361 mm. With 0.341 mm, the transition zone for the optimized strategy is slightly smaller. The starting point is a -0.161 mm and it ends at 0.180 mm. After applying the optimization strategy, both material transition zones had no observable defects and showed comparable dimensions. Thus, the experimental approach for adjusting the energy input in the build direction and determining the number of layers was proven. Ten and four layers were suitable to achieve a similar expansion for transitions from 1.2709 to CW106C and CW106C to 1.2709, respectively. Compared to the standard strategies, transition zone width reductions of 65% and 6%

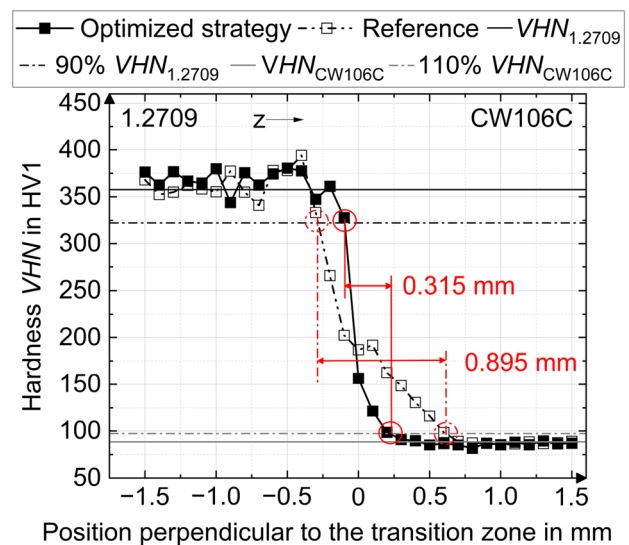


Fig. 8 Values of the Vickers hardness over the position perpendicular to the transition zone of CW106C build on 1.2709; the solid horizontal lines represent the mean VHN in the mono-material region and the dotted-dashed lines indicate a 10% deviation. The derived width of the transition zones are visualized by the arrows

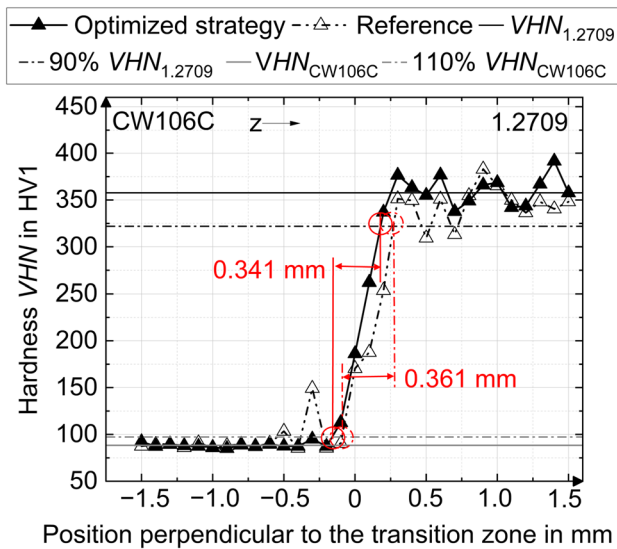


Fig. 9 Values of the Vickers hardness over the position perpendicular to the transition zone of 1.2709 build on CW106C; the solid horizontal lines represent the mean VHN in the mono-material region and the dotted-dashed lines indicate a 10% deviation. The derived width of the transition zones are visualized by the arrows

were achieved. The decreased energy input leads to smaller, shallower melt pools, which not only limits material mixing but also accelerates the solidification. This in turn fosters supersaturated mixed crystals and might mitigate hot cracks during the solidification.

4.2 Transition zone in the x–y plane

In Fig. 10, micrographs of the transition zone in the x–y plane for the reference according to Anstaett [16], manufactured with the starting parameters for the wobbling strategy (Parameter set 1 and 2, cf. Table 3), and with the parameter sets leading to the best results (Parameter set 7 and 8, cf. Table 3).

Figure 10a represents the reference according to Anstaett [16]. The transition zone exhibits defects and an irregular intermixing of the materials. For the samples in the Fig. 10b and c, wobbling parameters with two different radii (0.25 mm and 0.125 mm) were applied. The energy inputs were too high; thus, a strong crack formation was observed in the 1.2709 region parallel to the transition zone, and gas porosity occurred in the transition zone. Increasing the scan speed decreased the size of the crack in the 1.2709 region. However, only lowering the laser power and increasing the scan speed of the wobble parameters while keeping the radii constant sufficiently reduced the energy input and led to an improvement of the transition zones (see Fig. 10d and e). Changing the radius of the wobble path resulted in different expansion

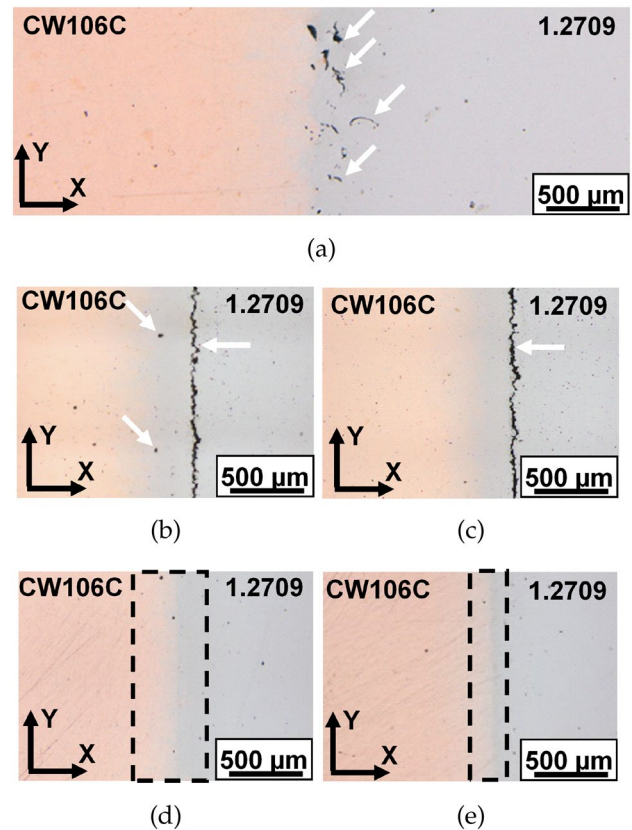


Fig. 10 Exemplary material transition zones in the x–y plane, **a** reference transition zone with the strategy according to Anstaett [16], **b–e** transition zone with the wobbling strategy: **b** parameter set 1, **c** parameter set 2, **d** parameter set 7, **e** parameter set 8 as described in Table 3

of the transition zones. With the 0.25 mm radius, a wider transition zone was achieved than with the radius of 0.125 mm.

The vertical cross sections in Fig. 11 confirms a defect-free formation of the transition zones over the entire build height of the two samples manufactured with the different radii during wobbling.

Hardness measurements were conducted for the two suitable wobble radii. The measurement values are plotted in Fig. 12 according to Sect. 4.1.

The transition zone for a wobbling radius of 0.250 mm starts at -0.471 mm and ends at 0.459 mm. This results in a width of 0.930 mm. Using a smaller radius of 0.125 mm leads to a narrower transition zone of 0.620 mm as already indicated by the micrographs. The transition zone intersects the starting threshold at -0.275 mm and ends at 0.345 mm. A further decrease of the wobble radius might lead to improved results for a smaller transition zone in the x–y plane.

By applying the wobbling strategy to the material transition in the x–y plane, otherwise occurring defects—in

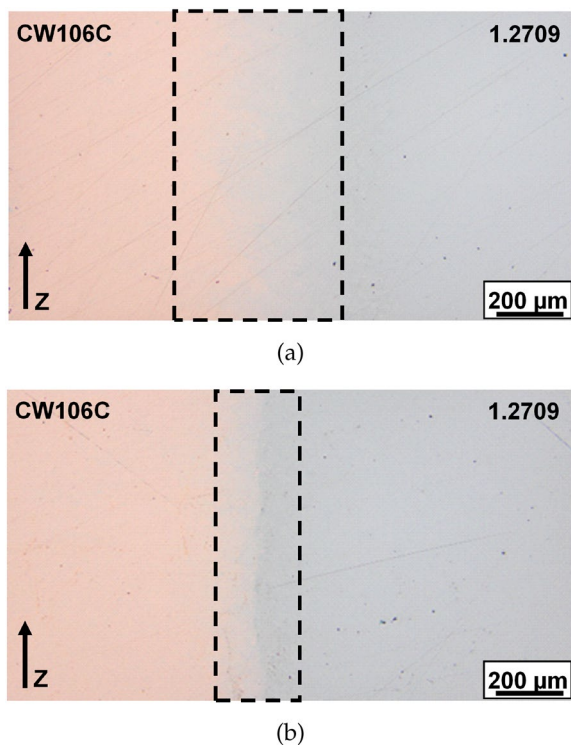


Fig. 11 a Wobbling radius 0.250 mm (parameter set 7, Table 3); b wobbling radius 0.125 mm (parameter set 8, Table 3)

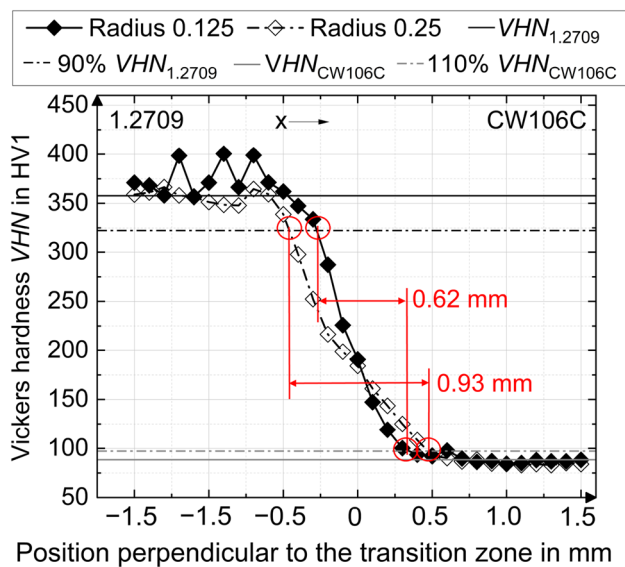


Fig. 12 Values of the Vickers hardness over the position perpendicular to the transition zone of 1.2709 next to CW106C; the solid horizontal lines represent the mean VHN in the mono-material region and the dotted-dashed lines indicate a 10% deviation. The derived width of the transition zones for both wobbling radii are visualized by the arrows

particular irregular porosity and hot cracks—could be avoided. A homogenization of the melting front and the melt pool in general by wobbling during re-melting appears to lead to healing effects of the re-melted area without causing new defects [31]. The energy input selected for wobbling seems especially critical as entirely new defects, such as stress cracks, may be created. For the investigated parameter variations, the width of the transition zone was four to five times the wobbling radius. Even though the general approach has been validated, a reduction of transition zone dimensions and a general wobbling geometry and a scanning parameter optimization need to be investigated in further studies.

4.3 Combined strategies for three-dimensional transition zones

For the validation of the 3D transition zone, both presented concepts were applied during the manufacturing of parts with transition zones at different angles using the stair step method.

The stair step height was varied to account for a sufficient accuracy while avoiding an overlap of the two building strategies in each direction.

The micrographs in Fig. 13 demonstrate the processability of the different step heights for both material build sequences at the angle of 45°.

The different step heights led to a variation in the discretization of the transition zone. The higher the steps, the more distinct are the transition zones. The extent of the steps is more pronounced for the build sequence of CW106C on 1.2709. For the other build sequence, the steps become blurred and more continuous. The smaller the steps, the stronger are the effects. The difference in the characteristics of the steps is also evident at different angles, which are depicted in Fig. 14. The samples were manufactured with a step height of 0.3 mm at different angles.

Discrete steps are visible in Fig. 14a. At all other angles, the transition zone blurs and becomes more continuous. However, for all variations few defects were detected and no cracks occurred.

To evaluate the feasibility and the applicability at different angles independent of the build sequences, the density was measured for each transition zone direction and for the three different step heights and are presented as mean values of both material build sequences. The densities of the references samples and the samples manufactured with the optimized strategy are summarized in Table 6.

For the evaluation of the optimized strategy, samples with a transition zone at an angle of 45° and a transition zone in the z-direction were built with the reference strategy *No overlap*. Additionally, samples at 22.5°, at 45°, at 67.5°, and in the x–y plane fabricated according to the strategy of

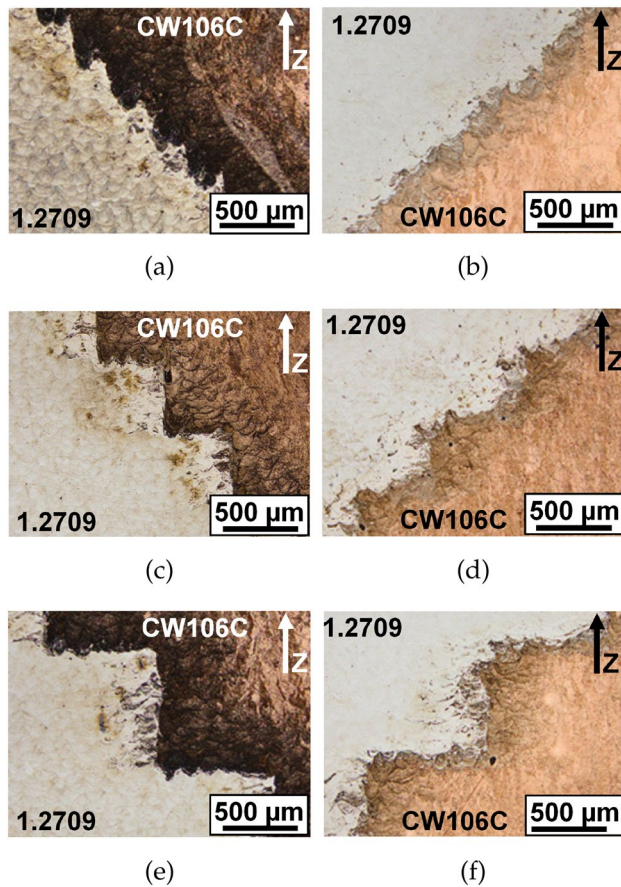


Fig. 13 Material transition zones with optimized step strategy for the transition zones at 45° for both material build sequences, **a** and **b** with a 0.3 mm step height, **c** and **d** with a 0.6 mm step height, **e** and **f** with a 0.9 mm step height

Anstaett [16] were analyzed. The density for mono-material parts with reprocessed powder from the multi-material process are listed according to Schroeder et al. [37] to be able to categorize the results of the transition zone.

Using the reference strategy *No overlap* in the z-direction led to comparable densities as in the monolithic regions. However, as soon as the transition zone angle changed,

defects were induced and the porosity rose. This effect is confirmed by measuring the density. The density values of the approach according to Anstaett [16] are suitable for the transition zone in the x–y plane. The smaller the angle, the higher is the porosity. Furthermore, the transition zone expansion increases with decreasing angles. Due to the constant overlap of 0.2 mm in the x–y plane, more areas of the two different materials imbricate [16].

With the optimized strategy, densities even higher than in the mono-material regions were achieved. This can be attributed to the healing effect of the wobbling strategy. However, when approximating a continuous transition by lowering the step size, strategies appear to interfere and porosity increases. The higher the steps, the fewer are the pores formed in the transition zone. The same effect was observed for an decreasing angle. The lower the angle, the fewer were the pores that occurred. Thus, a trade-off between the resolution of the process and defect-free transition zones arises. It can be summarized that the method can be applied for inclined material transitions. However, further energy input optimizations might be needed for fully continuous transition zones.

5 Conclusions and outlook

A general approach for creating transition zones with high fidelity in multi-material PBF-LB/M was developed and presented. It contains three major steps: a linear grading of the energy input in the build direction (z-direction) over a selectable number of layers, a homogenization of the transition zone within a single layer using wobbling during the re-melting, and a discretization of the inclined transition zones via specific increments to combine the first two steps. The method was validated using one of the most relevant material combinations in multi-material PBF-LB/M [1]. It has been shown that the method is suitable for manufacturing multi-material transitions, which are comparable to mono-material regions regarding the defect occurrence. A transition zone height (extent in the z-direction) of 341 μm

Table 6 Measured densities for the mono-material regions according to Schroeder et al. [37] and the different transition zone directions (dir.) for the three presented approaches compared to the manufacturing with no overlap and to the approach of Anstaett [16]

Mono-mat.	Reference [37]	<i>No overlap</i>	Reference [16]	Step approach with 3 heights		
CW106C	99.60%					
1.2709	99.73%					
Dir.				0.3 mm	0.6 mm	0.9 mm
z		99.69%	–	99.86%	99.86%	99.86%
22.5°		–	99.40%	99.72%	99.81%	99.90%
45°		99.37%	99.54%	99.51%	99.66%	99.75%
67.5°		–	99.59%	99.13%	99.38%	99.49%
x–y		–	99.63%	99.92%	99.92%	99.92%

The densities are shown as mean values of both material build sequences

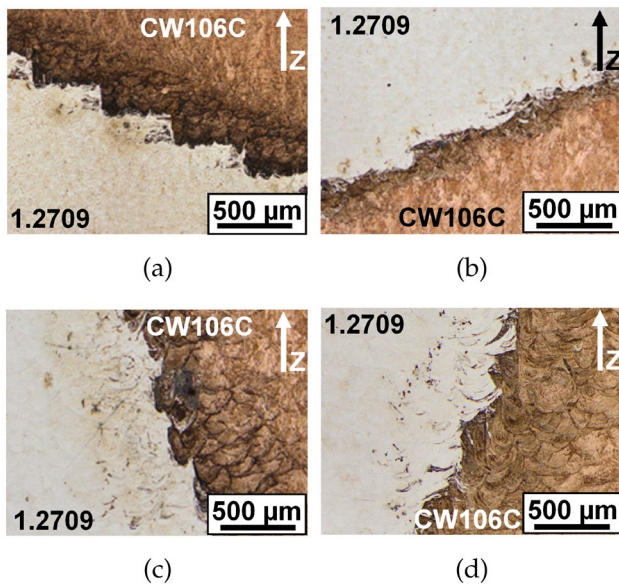


Fig. 14 Material transition zones with optimized step strategy for the transition zones with a 0.3 mm step height for both build sequences, **a** and **c** at the angle of 22.5°, **b** and **d** at the angle of 67.5°

and a width (extent in the x – y plane) of about 620 μm could be achieved. The healing effects of the re-melted area appear to enable low-defect material transitions in the x – y plane. Inclined transition zone quality was the highest for the largest steps and thus the lowest number of alterations between the transition zones in the z -direction and the x – y plane. Continuous approximation by decreasing the step size caused an increase in porosity.

Given the dimensions of the material transition achieved in this study, the method is currently limited to bulk material and not specifically suited for fine structures below approximately 341 μm (z -direction) and 620 μm (x – y plane). Upcoming investigations will focus on further decreasing the transition zone dimensions and lowering the step size of the inclined material transitions. To ensure that no unwanted phases form in the transition zone, X-ray diffraction measurements will be carried out. Additionally, mechanical investigations of multi-material test pieces manufactured by applying the presented approach will be conducted. The same applies to further validations by transferring the method to other material combinations.

Acknowledgements We hereby express our gratitude to the Freistaat Bayern and its Bavarian Ministry of Economic Affairs, Energy and Technology for the funding of this work, within the project MultiMat Bavaria II. The results in this paper were achieved within the scope of the research project ACCURACY (Grant No. RvS-SG20-3451-1/41/5).

Author contributions T. S.: conceptualization, methodology, investigation—performing experiments and analyzing data, writing—original draft, writing—review and editing, visualization. M. L.: conceptualization, writing—original draft, writing—review and editing. M. H.:

conceptualization, writing—original draft, writing—review and editing. P. K.: project administration, writing—review and editing. I. U.: project administration, writing—original draft, writing—review and editing. F. M.: investigation—performing experiments and analyzing data. A. L.: investigation—performing experiments and analyzing data. G. S.: methodology, writing—review and editing, funding acquisition. Resources, writing—review and editing, supervision, funding acquisition. C. S.: writing—review and editing, funding acquisition. Resources, writing—review and editing, supervision, funding acquisition. All authors have read and agreed to the published version of the manuscript.

Funding Open Access funding enabled and organized by Projekt DEAL.

Data and code availability Not applicable.

Declarations

Conflict of interest The authors declare that they have no conflict of interest.

Ethical approval Not applicable.

Open Access This article is licensed under a Creative Commons Attribution 4.0 International License, which permits use, sharing, adaptation, distribution and reproduction in any medium or format, as long as you give appropriate credit to the original author(s) and the source, provide a link to the Creative Commons licence, and indicate if changes were made. The images or other third party material in this article are included in the article's Creative Commons licence, unless indicated otherwise in a credit line to the material. If material is not included in the article's Creative Commons licence and your intended use is not permitted by statutory regulation or exceeds the permitted use, you will need to obtain permission directly from the copyright holder. To view a copy of this licence, visit <http://creativecommons.org/licenses/by/4.0/>.

References

- Schneck M, Horn M, Schmitt M, Seidel C, Schlick G, Reinhart G (2021) Review on additive hybrid-and multi-material-manufacturing of metals by powder bed fusion: State of technology and development potential. *Prog Addit Manuf* 6:1–14. <https://doi.org/10.1007/s40964-021-00205-2>
- DIN EN ISO/ASTM TR 52912:2020.: Additive manufacturing – Design – Functionally graded additive manufacturing. Beuth Verlag GmbH, Berlin
- Schneck M, Horn M, Schindler M, Seidel C (2022) Capability of multi-material laser-based powder bed fusion-development and analysis of a prototype large bore engine component. *Metals* 12(1):44. <https://doi.org/10.3390/met12010044>
- Ringel B, Zaepfel M, Herlan F, Horn M, Schmitt M, Seidel C (2022) Advancing functional integration through multi-material additive manufacturing: Simulation and experimental validation of a burner nozzle. *Mater Today Proc* 70(2):296–303. <https://doi.org/10.1016/j.matpr.2022.09.241>
- Kindermann P, Strasser M, Wunderer M, Uensal I, Horn M, Seidel C (2023) Cold spray forming: a novel approach in cold spray additive manufacturing of complex parts using 3D-printed polymer molds. *Prog Addit Manuf* 22:413. <https://doi.org/10.1007/s40964-023-00521-9>

6. Schmitt M, Gottwalt A, Winkler J, Tobie T, Schlick G, Stahl K et al (2021) Carbon particle in-situ alloying of the case-hardening steel 16mncr5 in laser powder bed fusion. *Metals* 11(6):896. <https://doi.org/10.3390/met11060896>
7. Lehmann M, Kolb CG, Gschloessl J, Zaeh MF (2023) Using particle-loaded inks to selectively change the material properties in binder-jetted WC-Co parts. *J Mater Sci* 58(41):16089–16104. <https://doi.org/10.1007/s10853-023-09023-z>
8. Binder M, Anstaett C, Horn M, Herzer F, Schlick G, Seidel C, et al. (2018) Potentials and challenges of multi-material processing by laser-based powder bed fusion. *Solid Freeform Fabric Proc*
9. Horn M, Schweiger J, Schroeder T, Langer L, Trimpl J, Erdelt K et al (2023) Additive Multimaterialfertigung von Metallen in der Doppelkronentechnik. *QZ - Quintessenz Zahntechnik*. 49(9):808–817
10. World Economic Forum. World Economic Forum, editor.: An additive manufacturing breakthrough: a how-to guide for scaling and overcoming key challenges. Available from: https://www3.weforum.org/docs/WEF_Additive_Manufacturing_Breakthrough_2022.pdf
11. DIN EN ISO/ASTM DIS 52900:2018.: Additive manufacturing – General principles – Terminology. Beuth Verlag GmbH, Berlin
12. Sing SL, Huang S, Goh GD, Goh GL, Tey CF, Tan JHK et al (2021) Emerging metallic systems for additive manufacturing: In-situ alloying and multi-metal processing in laser powder bed fusion. *Prog Mater Sci* 119:100795. <https://doi.org/10.1016/j.pmatsci.2021.100795>
13. Sun H, Chu X, Luo C, Chen H, Liu Z, Zhang Y et al (2021) Selective laser melting for joining dissimilar materials: investigations of interfacial characteristics and in situ alloying. *Metall Mater Trans A* 52(4):1540–1550. <https://doi.org/10.1007/s11661-021-06178-9>
14. Reichardt A, Shapiro AA, Otis R, Dillon RP, Borgonia JP, McEnerney BW et al (2021) Advances in additive manufacturing of metal-based functionally graded materials. *Int Mater Rev* 66(1):1–29. <https://doi.org/10.1080/09506608.2019.1709354>
15. VDI 3405.: Page 2.8, Additive manufacturing processes – Powder bed fusion of metal with laser beam (PBF-LB/M) – Defect catalogue – Defect images during laser beam melting, 2021-05. Beuth Verlag GmbH
16. Anstaett C, Multimaterialverarbeitung mittels Laserstrahlschmelzen am Beispiel von metallischen Verbindungen mit der Kupferlegierung CW106C [Dissertation]. Technische Universität München (2020)
17. Horn M, Langer L, Schafnitzel M, Dietrich S, Schlick G, Seidel C et al (2020) Influence of metal powder cross-contaminations on part quality in Laser Powder Bed Fusion: copper alloy particles in maraging steel feedstock. *Procedia CIRP* 94(3):167–172. <https://doi.org/10.1016/j.procir.2020.09.032>
18. Anstaett C, Seidel C, Reinhart G (2018) Multi-material fabrication of copper-chrome-zirconia and tool steel 1.2709 by powder bed based laser beam melting. *Fraunhofer Direct Digital Manufacturing Conference DDMC*
19. Anstaett C, Seidel C, Reinhart G (2017) Fabrication of 3D-multi-material parts by laser beam based powder bed fusion. *Solid Freeform Fabrication Proceedings*
20. Rankouhi B, Jahani S, Pfeifferkorn FE, Thoma DJ (2021) Compositional grading of a 316L-Cu multi-material part using machine learning for the determination of selective laser melting process parameters. *Addit Manuf* 38:101836. <https://doi.org/10.1016/j.addma.2021.101836>
21. Weissbach W, Werkstoffkunde: Strukturen, Eigenschaften, Prüfung. 17th ed. Wiesbaden: Vieweg + Teubner (2010) Available from: <http://dx.doi.org/10.1007/978-3-8348-9343-7>
22. Becker D (2014) Selektives Laserschmelzen von Kupfer und Kupferlegierungen [Dissertation]. RWTH Aachen University
23. Lu XY, Cao CD, Wei B (2001) Microstructure evolution of under-cooled iron-copper hypoperitectic alloy. *Mater Sci Eng A* 313(1–2):198–206. [https://doi.org/10.1016/S0921-5093\(01\)00928-5](https://doi.org/10.1016/S0921-5093(01)00928-5)
24. Munitz A (1987) Liquid separation effects in Fe–Cu alloys solidified under different cooling rates. *Metall Trans B* 18(3):565–575. <https://doi.org/10.1007/BF02654269>
25. Phanikumar G, Manjini S, Dutta P, Chattopadhyay K, Mazumder J (2005) Characterization of a continuous CO₂ laser-welded Fe-Cu dissimilar couple. *Metall Mater Trans A* 36(8):2137–2147. <https://doi.org/10.1007/s11661-005-0334-6>
26. Chen S, Huang J, Xia J, Zhang H, Zhao X (2013) Microstructural Characteristics of a Stainless Steel/Copper Dissimilar Joint Made by Laser Welding. *Metall Mater Trans A* 44(8):3690–3696. <https://doi.org/10.1007/s11661-013-1693-z>
27. Kauss N, Halle T, Rosemann P (2018) Age-hardening behaviour, microstructure and corrosion resistance of the copper alloyed stainless steel 1.4542. *IOP Confer Series Mater Sci Eng* 373:012020. <https://doi.org/10.1088/1757-899X/373/1/012020>
28. Yao C, Xu B, Zhang X, Huang J, Fu J, Wu Y (2009) Interface microstructure and mechanical properties of laser welding copper-steel dissimilar joint. *Optics Lasers Eng* 47(7–8):807–814. <https://doi.org/10.1016/j.optlaseng.2009.02.004>
29. Mai TA, Spowage AC (2004) Characterisation of dissimilar joints in laser welding of steel-kovar, copper-steel and copper-aluminium. *Mater Sci Eng A* 374(1–2):224–233. <https://doi.org/10.1016/j.msea.2004.02.025>
30. Wilhelm M (1999) Direktes selektives Laser Sintern einkomponentiger metallischer Werkstoffe [Dissertation]. RWTH Aachen University
31. Kuryntsev SV, Gilmudtinov AK (2015) The effect of laser beam wobbling mode in welding process for structural steels. *Int J Adv Manuf Technol* 81:1683–1691. <https://doi.org/10.1007/s00170-015-7312-y>
32. Heeling T, Gerstgrasser M, Wegener K (2017) Investigation of selective laser melting spatter characteristics for single- and multi-beam strategies using high speed imaging. *Proceedings of the Lasers in Manufacturing Conference (LiM 2017)*, Munich, Germany
33. VDI 3405.: Page 2.1, Additive manufacturing processes – Powder bed fusion of metals using a laser beam (PBF-LB/M) – Presentation of material properties in material data sheets, 2022-05. Beuth Verlag GmbH
34. VDI 3405.: Page 2, Additive manufacturing processes, rapid manufacturing – Beam melting of metallic parts – Qualification, quality assurance and post processing, 2013-08. Beuth Verlag GmbH
35. Schindelin J, Arganda-Carreras I, Frise E, Kaynig V, Longair M, Pietzsch T et al (2012) Fiji: an open-source platform for biological-image analysis. *Nat Methods* 9(7):676–682
36. DIN EN ISO 6507-1:2018-07.: Metallic materials – Vickers hardness test – Part 1: Test method. Beuth Verlag GmbH, Berlin
37. Schroeder T, Horn M, Kindermann P, Schmitt M, Schlick G (2022) Investigation of the Potentials and Current imitations of Multi-material Manufacturing of Metals by Powder Bed Fusion based on a Copper and Steel Material Combination. *World PM* 2022

Publisher's Note Springer Nature remains neutral with regard to jurisdictional claims in published maps and institutional affiliations.